ISSN (Print) 1226-1750
ISSN (Online) 2233-6656
Journal of Magnetics 31(1), 79-90 (2026) https://doi.org/10.4283/JMAG.2026.31.1.79

A Fast Hybrid Analytical Model of PM Machine with Halbach Magnets and Saturation Effects

Yan Zhu*, Tao Peng*, Chuanhui Zhu, and Congli Mei

College of Electrical Engineering, Zhejiang University of Water Resources and Electric Power, Hangzhou 310018, China

(Received 24 November 2025, Received in final form 8 January 2026, Accepted 8 January 2026)

Surface-mounted permanent magnet (SPM) machines using Halbach magnet arrays offer enhanced magnetic performance but are prone to increased magnetic saturation due to their assembled magnetic effects. This study aims to develop a hybrid analytical model that accurately predicts the electromagnetic behavior of Halbach-based SPM machines while accounting for magnetic saturation. The proposed approach couples the subdomain method with an equivalent magnetic network (EMN). The subdomain model computes the unsaturated air-gap field, and the EMN introduces equivalent surface currents at saturation-prone boundaries to represent the nonlinear permeability. The proposed model demonstrates excellent agreement with finite element method (FEM), with the average torque deviation below 5% while requiring only about 3% of the FEM computation time. Experimental measurements of a prototype further validate the accuracy of the analytical predictions. The hybrid model therefore provides a fast, accurate, and physically transparent tool for the analysis and design of Halbach-based SPM machines under magnetic saturation.

Keywords : saturation effect, Halbach magnet, subdomain model, equivalent magnetic network, equivalent surface current.

1. Introduction

Surface-mounted permanent magnet (SPM) machines are widely used in various fields such as industry, aerospace, and household appliances due to their simple structure, high power density, and high efficiency [1–3]. Halbach magnet arrays are often employed in SPM machines owing to their advantages of self-shielding magnetization, highly sinusoidal magnetic flux distribution, and low cogging torque [4, 5]. Increasing the number of magnet segments can further reduce magnetic field harmonics, which benefits torque production, reduces losses, and improves overall performance. However, some studies have reported that such structures may also reduce the fundamental component of the magnetic flux density, which in turn lowers the torque density of the machine [6, 7]. To address this issue, it is necessary not only to explore new machine topologies, but also to develop accurate electromagnetic field models.

There are two main approaches to achieve accurate electromagnetic modeling of SPM machines [8]. The first is the FEM, which is the most widely used due to its high computational precision and capability to model complex geometries. Although FEM provides accurate numerical solutions, it demands significant computational resources and acts as a numerical tool that provides limited physical insight for analytical adaptation [9–11]. The second approach involves analytical and semi-analytical modeling, which aims to balance clear physical meaning and computational efficiency. Typical examples include subdomain field models, equivalent magnetic network (EMN) methods, and hybrid approaches that combine analytical formulations with numerical correction techniques [12, 13]. Several subdomain models have been proposed for machines with Halbach magnetization. In [14], a subdomain model was developed for a flux-reversal machine with a Halbach array, where the analytical formulation was used to optimize torque by adjusting the magnetization angle. In [15], a subdomain model was applied to a slot-less SPM machine with segmented Halbach magnets, showing good agreement with FEM while requiring much less computation. It should be noted that both studies

---

©The Korean Magnetics Society. All rights reserved.

*Corresponding author: Tel: +86-17368756807
e-mail: zhuyan@zjweu.edu.cn
Tel: +86-13625841800
e-mail: pengt@zjweu.edu.cn

© 2026 Journal of Magnetics

focus on machine configurations in which magnetic saturation is weak, and the models are therefore built under the assumption of linear magnetic material properties. To consider magnetic saturation, [16] extended the subdomain model to a multiphase Halbach-array axial-flux PM machine by introducing Laplacian equations in the iron subdomains instead of assuming infinite permeability. Although this approach improves accuracy under saturated conditions, it also increases the number of subdomains and boundary conditions, making the model more complex and less convenient to adapt to other machine configurations. Overall, existing subdomain models for Halbach machines either neglect magnetic saturation or include it through topology-specific extensions that significantly increase modeling complexity. This motivates the development of a more general analytical framework that can account for saturation effects while keeping the model compact and easy to extend.

In parallel, EMN models have also been widely applied for electromagnetic analysis of PM machines. In [17], a permeance network model was developed for PM machines with complex geometric structures. The magnetic circuit is discretized into basic elements for electromagnetic analysis, and magnetic saturation is considered through permeability updating. In [18], an EMN-based model was proposed for a fractional-slot L-shaped vernier PM machine. The model constructs the magnetic network using structured permeance elements and supports performance evaluation of the target topology. In [19], an EMN-based model with multiple element types was developed for a dual three-phase vernier PM machine. Magnetic flux sources, reluctances, and magductances are used to represent rotor motion and loss-related effects, and saturation is incorporated through an effective magnetic impedance. Overall, existing EMN-based approaches describe electromagnetic behavior using discretized magnetic networks with lumped parameters. The magnetic field distribution is therefore represented in a lumped form rather than in a continuous analytical form. This representation limits direct access to continuous field information, which is often required for analytical field analysis and harmonic evaluation. Along this line, hybrid modeling approaches have been introduced to extend analytical formulations by incorporating numerical treatments. In [20], a hybrid analytical model was proposed for a flux reversal PM machine with asymmetric stator poles, combining the subdomain method with the Schwarz-Christoffel transformation to account for slotting effects of both stator and rotor. Nevertheless, due to the lack of magnetic saturation consideration, the model demonstrated good accuracy only under low-load and rated-load conditions. In [21], a hybrid approach combining the Fourier model and FEM was introduced, incorporating magnetic saturation effects. Applied to a simple SPM machine, this method achieved reduced computation time while maintaining high accuracy compared to pure FEM.

Despite these developments, analytical modeling of Halbach array SPM machines continues to focus on two practical aspects. One is to keep the analytical formulation compact while avoiding excessive growth in complexity. The other is how magnetic saturation can be incorporated into analytical modeling. To explore these aspects, this paper proposes a hybrid analytical framework that couples the subdomain field solution with a nonlinear EMN through an equivalent boundary current formulation. The introduced surface currents represent magnetic potential drops at regions prone to saturation and allow magnetic saturation to be included while keeping the original subdomain structure unchanged. In Section 2, the machine topology and the on-load subdomain model are introduced. Section 3 presents the hybrid analytical model by integrating the subdomain method with the EMN approach, along with the complete solution flowchart. In Section 4, analytical results are validated through comparison with both FEM simulations and experimental measurements. Finally, the conclusions are drawn in Section 5. The main contributions of the paper can be summarized as follows. First, a hybrid analytical modeling framework is developed by coupling the subdomain analytical formulation with a nonlinear EMN. The coupling mechanism introduces equivalent surface currents at saturation-prone boundaries. It enables the analytical model to account for magnetic saturation while maintaining computational efficiency. Second, the proposed framework is extended to the analysis of Halbach-array SPM machines. It provides an accurate and physically transparent tool for investigating their electromagnetic characteristics under nonlinear operating conditions.

2. On-Load Subdomain Model

In this section, an on-load subdomain model is established as the foundation of the hybrid analytical model, excluding magnetic saturation at first. Fig. 1(a) present the topology of the SPM machine. The machine features a 9-slots, 8-poles configuration with three-segment Halbach magnets. The distribution of the armature windings and the associated phase currents is detailed in Fig. 1(b). A three-phase concentrated winding type is applied to the machine and current flow directions are

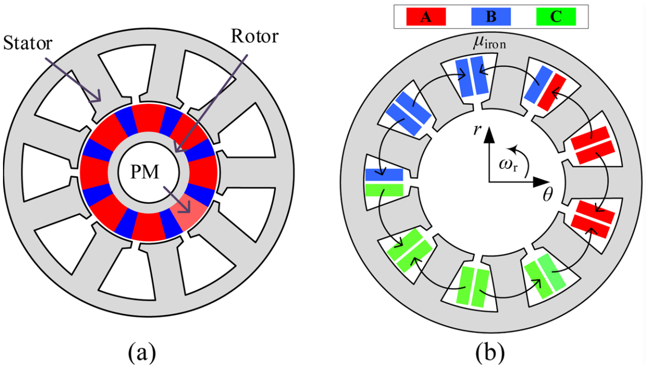

(a) (b)

Fig. 1. (Color online) SPM machine. (a) machine topology. (b) Winding layout.

also indicated. Key design parameters of the machine are summarized in Table 1. Although the target machine studied in this paper adopts a Halbach magnetization pattern, the subdomain formulation presented in this section is written in a general form for SPM machines. The analytical structure of the governing equations does not depend on a specific magnetization pattern. The Halbach configuration is introduced subsequently through the explicit definition of the magnetization distribution. In this way, the proposed formulation preserves generality while being readily specialized to Halbach-array SPM machines.

The machine is divided into four subdomains: stator slots, stator slot openings, air-gap and PMs, as illustrated in Fig. 2(a). The corresponding geometric parameters of the subdomain model are depicted in Fig. 2(b). To facilitate analytical derivation and improve computational efficiency, the following assumptions are made:

1) End effects are neglected.

2) All materials are assumed to be isotropic and homogenous.

Table 1. Specifications of the SPM machine.

Item	Symbol	Value
Rated power (W)	P_{N}	260
Rated speed (r/min)	n_{N}	4000
PM pole-pairs	p_{r}	4
Number of slots	Ns	9
Stator outer diameter(mm)	D_{os}	95
Stator inner diameter (mm)	D_{is}	46
Rotor outer diameter(mm)	D_{or}	45
Rotor inner diameter (mm)	D_{ir}	26
Axial length (mm)	l_{ef}	60
Number of turns per slot	N_1	4
PM thickness (mm)	l_{pm}	9
Slot width (°)	b_{s}	23
Slot opening (°)	b_{o}	6.36
Stator yoke width (mm)	w_{sy}	5.6
PM material	/	NdFe35 (B_r=1.23)
Iron core material	/	B20AT1500 (stacking factor=0.97)

3) Eddy current effects are not taken into account.

Based on Maxwell's equations and the Coulomb gauge condition, the governing equation of the magnetic vector potential is derived as follows:

$$\begin{cases}\nabla^2 \boldsymbol{A} = 0, \text{ source free area} \\ \nabla^2 \boldsymbol{A} = -\mu_0\mu_r \boldsymbol{J} - \mu_0 \nabla \times \boldsymbol{M}, \text{ source area}\end{cases} \tag{1}$$

where $\boldsymbol{A}$, μ_0, μ_r, $\boldsymbol{J}$ and $\boldsymbol{M}$ represent the magnetic potential vector, the vacuum permeability, the relative permeability, the current density vector and the magnetization vector, respectively. According to (1), the magnetic vector potential in the 2-D coordinate can be expressed as

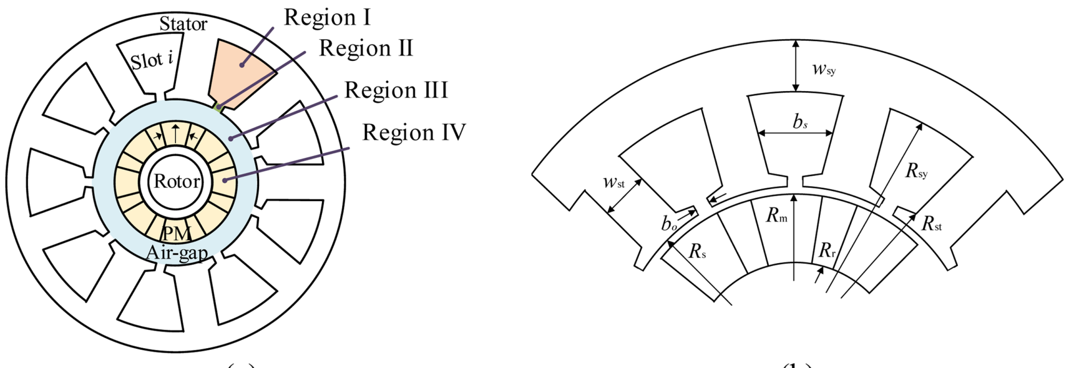

(a) (b)

Fig. 2. (Color online) Definitions of subdomains. (a) subdomains. (b) geometric parameters.

$$\begin{cases} \dfrac{\partial^2 A(r,\theta)}{\partial r^2}+\dfrac{1}{r}\dfrac{\partial A(r,\theta)}{\partial r}+\dfrac{1}{r^2}\dfrac{\partial^2 A(r,\theta)}{\partial \theta^2}=0, \text{ source free area} \\ \dfrac{\partial^2 A(r,\theta)}{\partial r^2}+\dfrac{1}{r}\dfrac{\partial A(r,\theta)}{\partial r}+\dfrac{1}{r^2}\dfrac{\partial^2 A(r,\theta)}{\partial \theta^2}=-\mu_0 \boldsymbol{J}, \text{ slot area} \\ \dfrac{\partial^2 A(r,\theta)}{\partial r^2}+\dfrac{1}{r}\dfrac{\partial A(r,\theta)}{\partial r}+\dfrac{1}{r^2}\dfrac{\partial^2 A(r,\theta)}{\partial \theta^2}=\dfrac{\mu_0}{r}(\dfrac{\partial M_r}{\partial \theta}\text{-}M_\theta), \text{ magnet area} \end{cases} \tag{2}$$

The term on the right-hand side corresponding to the magnet area accounts for the magnetization distribution in the magnet, where the tangential component M_θ is assumed to be radially uniform.

In the considered SPM machine, the source free areas include the air-gap subdomain and the stator slot opening subdomain, while the source areas comprise the stator slot subdomain and the PM subdomain. In the stator slot subdomain, the sources consist of both armature currents and the equivalent surface currents. By applying the interface conditions between adjacent subdomains and iron cores, the magnetic vector potential in the stator slots, slot openings, air-gap and PMs can be derived from (2) as follows:

$$A_{IIi}(r,\theta)=\sum_m [A_{2i}(\frac{r}{R_{st}})^{-F_m}+B_{2i}(\frac{r}{R_s})^{F_m}]\cos[F_m(\theta+\frac{b_o}{2}-\theta_i)] \tag{3}$$

for the i^{th} slot openings in Region II, and

$$A_{III}(r,\theta)=\sum_k [A_3(\frac{r}{R_s})^{k}+B_3(\frac{r}{R_m})^{-k}]\cos(k\theta) + \sum_k [C_3(\frac{r}{R_s})^{k}+D_3(\frac{r}{R_m})^{-k}]\sin(k\theta) \tag{4}$$

for air-gap in Region III, and

$$A_{IV}(r,\theta)=\sum_k [A_4(\frac{r}{R_m})^{k}+B_4(\frac{r}{R_r})^{-k}]\cos(k\theta) + \sum_k [C_4(\frac{r}{R_m})^{k}+D_4(\frac{r}{R_r})^{-k}]\sin(k\theta)+f_2(k) \tag{5}$$

for PM in Region IV, where $F_m = m\pi/b_o$. θ_i is the position of i^{th} stator slot and

$$f_2(k)=\sum_k \frac{\mu_0 r(kM_{rsk}-M_{\alpha ck})}{1-k^2}\cos(k\theta)-\sum_k \frac{\mu_0 r(kM_{rck}+M_{\alpha sk})}{1-k^2}\sin(k\theta) \tag{6}$$

where M_{rsk} and M_{rck} denote the sine and cosine components of the radial magnetization, and $M_{\mathrm{\alpha ck}}$ and $M_{\mathrm{\alpha sk}}$ correspond to the sine and cosine components of tangential magnetization for the k^{th}-order harmonics [21]. For the Halbach-array SPM machine considered in this study, the radial and tangential magnetization distributions are illustrated in Fig. 3. Their corresponding components are given as:

$$\begin{cases} M_{rck}=M_{rk}(k)\cos(k\omega_r t+k\theta_0) \\ M_{rsk}=M_{rk}(k)\sin(k\omega_r t+k\theta_0) \\ M_{\theta ck}=-M_{\theta k}(k)\sin(k\omega_r t+k\theta_0) \\ M_{\theta k}=M_{\theta k}(k)\cos(k\omega_r t+k\theta_0) \end{cases} \tag{7}$$

where M_{rk} and $M_{\mathrm{\alpha k}}$ are Fourier coefficients of the radial and tangential magnetization components, respectively. θ_0 and ω_{r} are the initial position of the rotor and the rotor rotational speed. Different magnetization patterns can be incorporated into the same analytical framework by modifying the corresponding Fourier coefficients in (7).

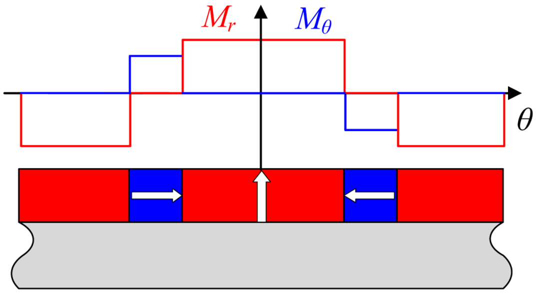

Fig. 3. (Color online) Magnetization of the SPM machine.

General solution for the stator slot subdomain must account for the boundary conditions at the interface with the iron core, where equivalent surface currents are imposed. The equation is derived as:

$$A_{Ii}(r,\theta)=\sum_n A_{1i}[G_1(\frac{r}{R_{\mathrm{sy}}})^{-F_n}+(\frac{r}{R_{\mathrm{st}}})^{F_n}]\cos[F_n(\theta+\frac{b_s}{2}-\theta_i)]+f_1(n) \tag{8}$$

for the i^{th} stator slots in Region I, where $G_1=(R_{sy}/R_{st})^{Fn}$ and $F_n = n\pi/b_s$. b_{s} is the width of stator slots. Moreover,

$$f_1(n)=\sum_n [\frac{F_n^2 X_n r}{1-F_n^2}-\frac{F_n X_n R_{sy}}{1-F_n^2}(\frac{r}{R_{sy}})^{-F_n}]\cos[F_n(\theta+\frac{b_s}{2}-\theta_{i1})] - \frac{\mu_0(J_{n1}+J_{n2})r}{b_s}+B_{ni}\ln r+0.25\mu_0 \mathbf{J}_{\mathbf{i}}(i)(2R_{sy}{}^2\ln r-r^2) \tag{9}$$

$$X_n=\frac{2\mu_0}{F_n^2 b_s}\{-(J_{n1}+J_{n2})(-1)^n\}+J_{n2}[(-1)^n-1] \tag{10}$$

$$B_{ni}=R_{sy}\mu_0(J_{n3}+\frac{J_{n1}+J_{n2}}{b_s}) \tag{11}$$

where A_{1i} represents the Fourier coefficients determined by the boundary conditions. J_{n1}, J_{n2} and J_{n3} are equivalent surface current calculated using the EMN in Section 3. $\mathbf{J}_\text{i}$ denotes the armature current density matrix, which can be calculated as:

$$\mathbf{J}_\text{i} = \frac{N_c \mathbf{C}_\text{i}}{A_c}[i_a \quad i_b \quad i_c] \tag{12}$$

where N_c, A_c and $\mathbf{C}_\text{i}$ represent coil turns, slot coil area and means the distribution matrix of armature windings obtained from Fig. 1(b), respectively.

The flux density in each subdomain can be derived from the magnetic vector potential as follows:

$$\begin{cases} B_r = \dfrac{1}{r}\dfrac{\partial A_z}{\partial \theta} \\ B_\theta = -\dfrac{\partial A_z}{\partial r} \end{cases} \tag{13}$$

The boundary conditions between stator slot and slot opening are given as:

$$\begin{cases} A_{Ii}|_{r=R_{st}} = A_{IIi}|_{r=R_{st}} \\ H_{Ii\theta}|_{r=R_{st}} = H_{IIi\theta}|_{r=R_{st}} \end{cases} \tag{14}$$

The boundary conditions between air-gap and stator slot openings are given as

$$H_{III\theta}|_{r=R_s} = \begin{cases} H_{IVi\theta}|_{r=R_s}, \theta_i - \dfrac{b_o}{2} < \theta < \theta_i + \dfrac{b_o}{2} \\ 0, \text{ elsewhere} \end{cases} \tag{15}$$

$$A_{III}|_{r=R_s} = A_{IIi}|_{r=R_s} \tag{16}$$

The boundary conditions between PM and air-gap are given as

$$\begin{cases} B_{IIIr}|_{r=R_m} = B_{IVr}|_{r=R_m} \\ H_{III\theta}|_{r=R_m} = H_{IV\theta}|_{r=R_m} \end{cases} \tag{17}$$

By solving the set of equation (10)-(13), the unknown constants in the magnetic vector potential expressions can be determined.

The analytical model in this section is based on the classical on-load subdomain formulation developed in [22], which is applicable to general SPM machines. In the present work, this formulation is specialized to a Halbach-array SPM through the introduction of the corresponding magnetization harmonics. Therefore, the analytical structure remains general, while the magnetization-related terms encode the specific Halbach configuration. This formulation provides a unified and consistent basis for coupling with the equivalent magnetic network introduced in the next section.

3. Hybrid Analytical Model

The magnetic vector potential distributions in different regions are obtained using the on-load subdomain model developed in Section 2. Based on these results, the air-gap and PM flux density are calculated, which are then used to derive the magnetic flux entering the stator teeth and the rotor yoke. The EMNs of the stator and the rotor, as illustrated in Fig. 4, are constructed to account for the nonlinear permeability of the iron core. Meanwhile, the isotropy and homogeneity assumptions remain valid. The network consists of 113 nodes and 122 permeance elements. The EMN is first divided along the dominant magnetic flux paths. Each permeance element is defined to represent a region with approximately uniform magnetic state. As indicated by the flux distribution in Fig. 5(a), stator teeth and the yoke sections between adjacent teeth satisfy this condition and is equal to one permeance. In these regions, further subdivision does not alter the magnetic field circulation or the global flux distribution. Additional refinement therefore leads to negligible improvement in prediction accuracy. The corresponding permeance can be expressed as:

$$\begin{cases} G_{s\_tooth} = \dfrac{\mu_0 \mu_r w_{st} l_{ef}}{l_{st}} \\ G_{s\_yoke} = \dfrac{\mu_0 \mu_r l_{ef}}{\theta_{sy}} \ln \dfrac{R_{sy} + w_{sy}}{R_{sy}} \end{cases} \tag{18}$$

where l_{st} is the length of one stator tooth and θ_{sy} is the angle between two adjacent teeth center lines.

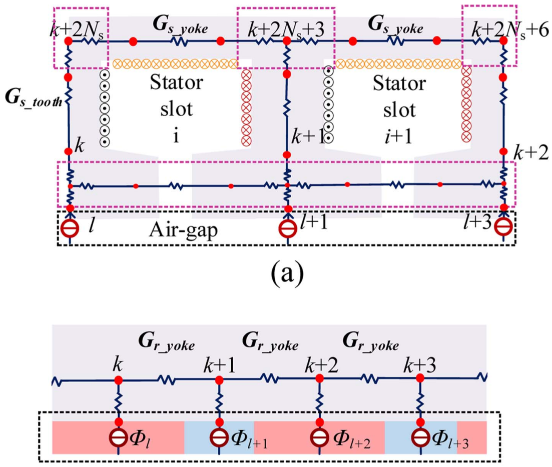

(a)

(b)

Fig. 4. (Color online) EMN. (a) stator. (b) rotor.

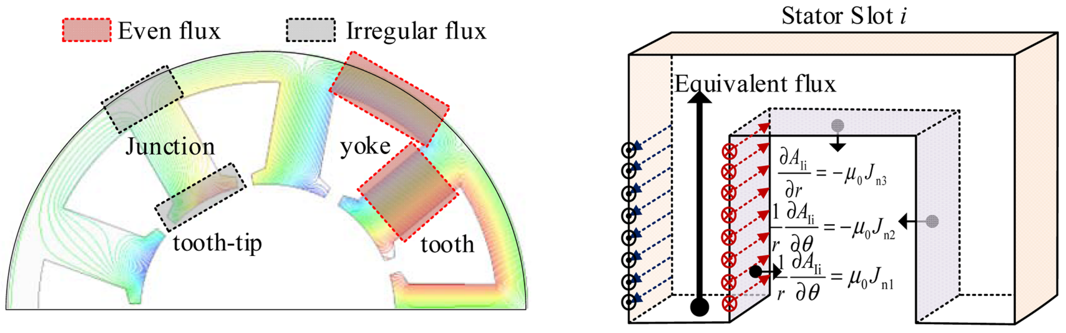

(a) (b)

Fig. 5. (Color online) Flux. (a) Flux distribution. (b) Saturation equivalent method.

The yoke section in the rotor is also equal to one permeance between two adjacent PMs and can be expressed as:

$$G_{r\_yoke} = \frac{\mu_0 \mu_r l_{ef}}{\theta_{ry}} \ln \frac{R_m}{R_r} \tag{19}$$

where θ_{ry} is the angle between two adjacent PMs center lines.

The MMF of the permanent magnet can be expressed as:

$$F_{pm} = H_c h_{pm} = \frac{B_r h_{pm}}{\mu_{pm} \mu_0} \tag{20}$$

where H_c is the coercive force of the PM, h_{pm} is the thickness of the PM, B_r is the remanence density of PM and μ_{pm} is the relative permeability.

By contrast, the tooth-tip region and the tooth-yoke junction have strong flux bending and nonuniform distribution. These regions are sensitive to local saturation and flux redistribution and are thus modeled using combined radial and tangential permeances. Based on this segmentation criterion, the EMN configuration with 113 nodes provides sufficient resolution to capture dominant flux paths and local saturation effects without unnecessary computational overhead. In addition, previous study has adopted the same method and confirmed its accuracy [23]. The chosen representation provides both high efficiency and reliable precision. In contrast, the flux distribution within the tooth-tip and the tooth-yoke junction is more irregular. This flux behavior directly influences the EMN design. As shown in Fig. 5(b), the saturation effect is accounted for by introducing equivalent surface currents at subdomain boundaries. Under magnetic saturation, the finite permeability of the iron core produces a non-negligible magnetic field intensity inside the iron. This leads to an additional magnetic potential drop along the main flux path. From the perspective of Maxwell's equations, a magnetic potential drop can be enforced by an additional circulation of magnetic field intensity. Such a circulation can be equivalently imposed by an additional current source. In this work, the saturation-induced magnetic potential drop is represented by surface current densities applied at subdomain boundaries. These equivalent surface currents generate the same magnetic field circulation as that caused by saturation and adjust the magnetic flux distribution accordingly. Initially, the equivalent surface currents are set to 0A, and their values are iteratively updated based on the EMN solution. The boundaries where these currents are applied are selected according to the locations prone to magnetic saturation.

The permeance matrix is initially assigned predefined values prior to the convergence process. Subsequently, the magnetic potential at each node is computed by applying ohm's law for magnetic circuit, and is given as:

$$\mathbf{F} = \frac{\mathbf{\Phi}}{\mathbf{G}} \tag{21}$$

where **F**, **Φ** and **G** means the magnetic potential matrix, the node flux matrix and the permeance matrix, respectively. Based on (14), the flux density at each permeance is obtained as:

$$B_{a,b} = \frac{F(a) - F(b)}{S_{a,b}} G(a,b) \tag{22}$$

where $B_{a,b}$ represents the flux density between node a and node b. $S_{a,b}$ represents the effective area of the permeance. The complete flowchart of the hybrid model is presented in Fig. 6. First, the on-load subdomain model is established, with an initial value of the equivalent surface current set to 0A for the first iteration. Based on this model, the magnetic flux entering the stator teeth and

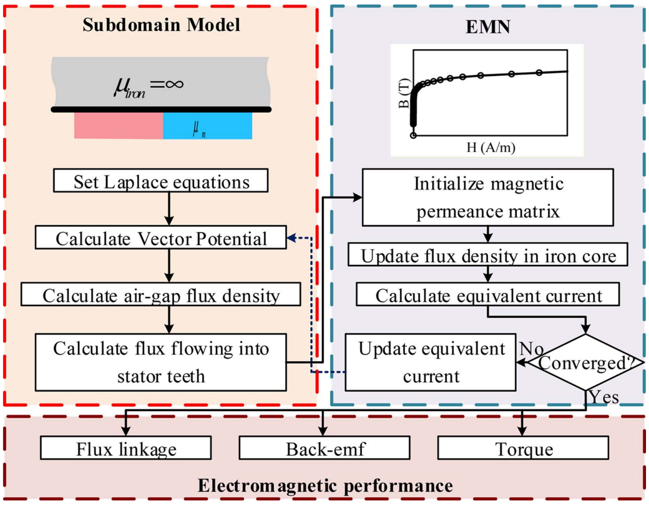

Fig. 6. (Color online) Flowchart of the hybrid analytical model.

rotor yoke is calculated and used as the input for the EMN. At the initial iteration, the magnetic permeance matrix is also initialized. The flux density in the iron cores and the corresponding equivalent surface currents is then updated iteratively. The convergence of the EMN is evaluated by comparing the flux density between successive iterations. The mathematic criterion for convergence is expressed as:

$$\max |B_k^p - B_k^{p-1}| < \lambda_B \quad (k = 1,2,3...) \tag{23}$$

where B_k^p, B_k^{p-1} and λ_B mean the present flux density, the previous flux density and the deviation limit, respectively. If the EMN model has not yet converged, the equivalent surface currents must be updated. The updated values are calculated as follows:

$$\begin{cases} J_{n1}^i = \dfrac{F(k+2N_s) - F(k)}{l_t} \\ J_{n2}^i = \dfrac{F(k+1) - F(k+2N_s+3)}{l_t} \\ J_{n3}^i = \dfrac{F(k+2N_s) - F(k+2N_s+3)}{l_y} \end{cases} \tag{24}$$

where l_t and l_y mean effective lengths of the tooth permeance and the yoke permeance. The convergence of the hybrid model is similar to the judgement of the EMN and is given as

$$\max |J_k^p - J_k^{p-1}| < \lambda_J \quad (k = 1,2,3...) \tag{25}$$

where J_k^p, J_k^{p-1} and λ_J mean the present equivalent surface current, the previous equivalent surface current and the deviation limit, respectively. After completing the iteration at a given rotor position, the electromagnetic performance can be obtained. The rotor is then advanced to the next position, and the above procedure is repeated. The computational procedure shown in Fig. 6 was implemented in MATLAB for iterative solution and data processing.

4. FEM and Experiment Demonstration

This section aims to verify the accuracy and computational efficiency of the proposed hybrid model. First, the analytical results are compared with those obtained from FEM. The FEM model was developed based on Maxwell's equations implemented in ANSYS Maxwell. Geometry of the FEM model follows Table 1. The model incorporates the non-linear magnetic properties of the iron cores as shown in Fig. 7(a). The magnetic flux density

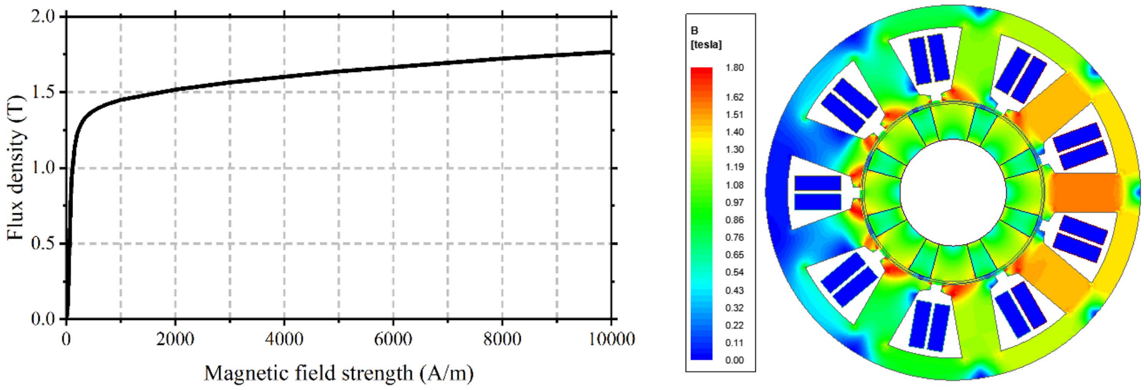

(a) (b)

Fig. 7. (Color online) FEM model. (a) B-H curve of iron cores. (b) Magnetic field distribution.

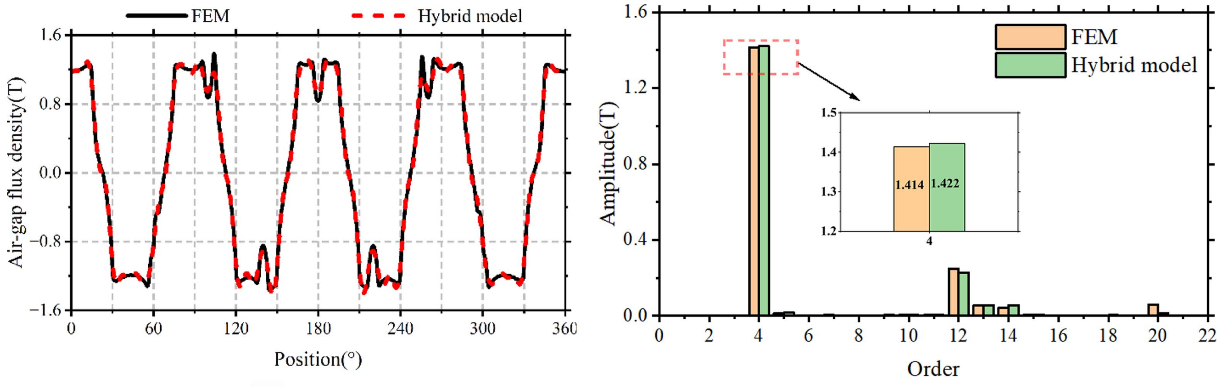

(a) (b)

Fig. 8. (Color online) Air-gap flux density. (a) Curve. (b) Harmonic distribution.

distribution at rated-load is illustrated in Fig. 7(b), where regions of high flux density and local saturation can be observed. The B–H curve of the laminated steel used for the stator and rotor cores was obtained from the manufacturer.

Both the numerical difference and computational costs are evaluated. The test condition involves a rotational speed of 4000 r/min and an armature current amplitude of 10 A. As shown in Fig. 8, the air-gap flux density and its harmonic components are compared between the hybrid model and the FEM results. A detailed comparison of the harmonic amplitudes is presented in Table 2. The deviation of the dominant 4th harmonic is only 0.6%. Although the higher-order harmonics exhibit larger relative deviations, their absolute amplitudes are significantly smaller than that of the dominant component. Specifically, the amplitudes of the 14th and 20th harmonics are below 5% of the dominant harmonic. Even under a conservative assumption that the contribution of a harmonic to electromagnetic torque scales proportionally with its amplitude, the maximum possible influence of these higher-order harmonics on the total torque is therefore bounded within a few percent. Consequently, the observed discrepancies in higher-order harmonic amplitudes do not lead to a noticeable degradation in the predicted torque and flux performance. The flux density distribution predicted by the hybrid model shows good agreement with the FEM results.

According to Stokes' theorem, the flux linkage in a stator slot can be expressed as:

$$\Phi_1 = N\oint_{\Gamma} A dl = N l_{ef}\frac{N_s}{S_t}\int_{R_{sy}}^{R_{st}}\int_{\theta_i-\frac{b_s}{2}}^{\theta_i+\frac{b_s}{2}} A_{Ii} r dr d\theta \tag{26}$$

where l_{ef} means the axial length, N means slot numbers of one phase and S_{t} means the area of a stator slot. By aggregating the flux linkage related to all slots placing coils of the identical phase, the total flux linkage Φ_1 of the phase is obtained.

Table 2. Comparison of harmonic amplitudes.

Harmonic	FEA model	Hybrid model	Deviation
4	1.414	1.422	0.6%
12	0.250	0.227	9.2%
13	0.055	0.056	1.8%
14	0.041	0.056	36.6%
20	0.058	0.016	72.4%

The electromagnetic torque is achieved as follows:

$$T_{\mathrm{e}} = \frac{l_{\mathrm{ef}} r^2}{\mu_0}\int_0^{2\pi} B_{\mathrm{IIIr}} B_{\mathrm{III\theta}} d\theta \tag{27}$$

It should be noted that (20) can also be used to calculate the cogging torque by substituting the on-load air-gap flux density with the no-load air-gap flux density. A comparative analysis was conducted under both linear and non-linear saturation conditions, as shown in Fig. 9. The results of the linear FEM, non-linear FEM, and the proposed hybrid model are summarized in terms of flux linkage and electromagnetic torque. For flux linkage, the linear FEM gives a peak value of 0.0113 Wb, the non-linear FEM gives 0.0108 Wb, and the hybrid model gives 0.0108 Wb. The linear FEM result is about 4.6% higher due to the neglect of magnetic saturation. For electromagnetic torque, the linear FEM produces 642.6 Nm, the non-linear FEM gives 620.3 Nm, and the hybrid model yields 632.8 Nm. The higher torque predicted by the linear FEM originates from the overestimated air-gap flux density. The torque of the hybrid model is slightly higher than the non-linear FEM result, with a deviation of about

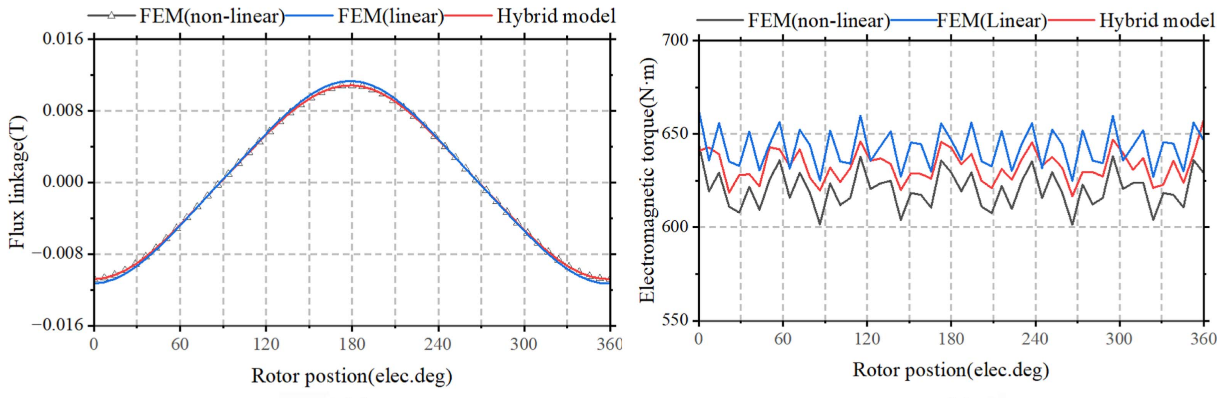

(a) (b)

Fig. 9. (Color online) Electromagnetic performance. (a) Flux linkage. (b) Electromagnetic torque.

Table 3. Comparison of computational consumptions.

Terms	FEM model	Hybrid model
server configuration	AMD Ryzen 5 7500F (3.70 GHz), 32GB memory	
Meshing nodes	69433	76
Occupied memory (MB)	520	1000
CPU time (sec)	300	10
Flux linkage difference (%)	/	0
Average torque difference (%)	/	2

2%, mainly caused by the simplified magnetic network. Local saturations near the tooth corner and slot opening are not considered in the model. Overall, the hybrid model reproduces the non-linear FEM behavior with good accuracy.

The detailed computational costs, including calculation time and memory usage for one electrical period, are summarized in Table 3. The mesh quality of the FEM model is illustrated in Fig. 10. The FEM mesh was optimized to achieve a balance between accuracy and computational cost. The element size in the air-gap and magnet regions was refined until the variation of average torque became less than 1% between two refinements, resulting in a final model with 69,433 nodes. The computation time of the hybrid model is approximately 3% of that required by the FEM model. In addition, the average torque deviation between the two methods indicates high accuracy of the hybrid model. These results demonstrate that the proposed hybrid model achieves both high computational efficiency and reliable precision.

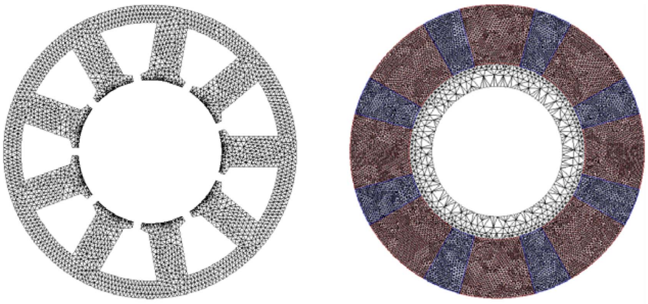

(a) (b)

Fig. 10. (Color online) FEM mesh plot. (a) stator. (b) rotor.

The experimental platform, as shown in Fig. 11(a), consists of a prototype machine, a DC machine, a torque sensor, an oscilloscope, a power supply and a Mitsubishi FR-A800 vector control inverter, which supports both induction and PM machine with field-oriented control. Experiments are conducted at a rotational speed of 4000 rpm under a rated phase current amplitude of 10 A. The measured phase back-EMF waveform is shown in Fig. 11(b). Both the complete and enlarged views are provided for clarity, with a vertical scale of 5 V/div and a time scale of 10 ms/div. The measured phase current and torque waveforms are illustrated in Fig. 11(c), including an enlarged view to highlight the waveform details, with vertical scales of 3 A/div for the phase current and 1.2 N·m/div for the torque.

The analytical back-EMF is calculated using Maxwell's second equation, as follows:

$$E=-\frac{d\Phi}{dt} \tag{28}$$

As shown in Fig. 12, the analytically predicted back-EMF and electromagnetic torque exhibit good agreement with both the FEM simulation results and the experimental measurements. This consistency validates the model's ability to reliably capture the machine's electromagnetic behavior under practical operating conditions.

Under no-load conditions, the influence of stator

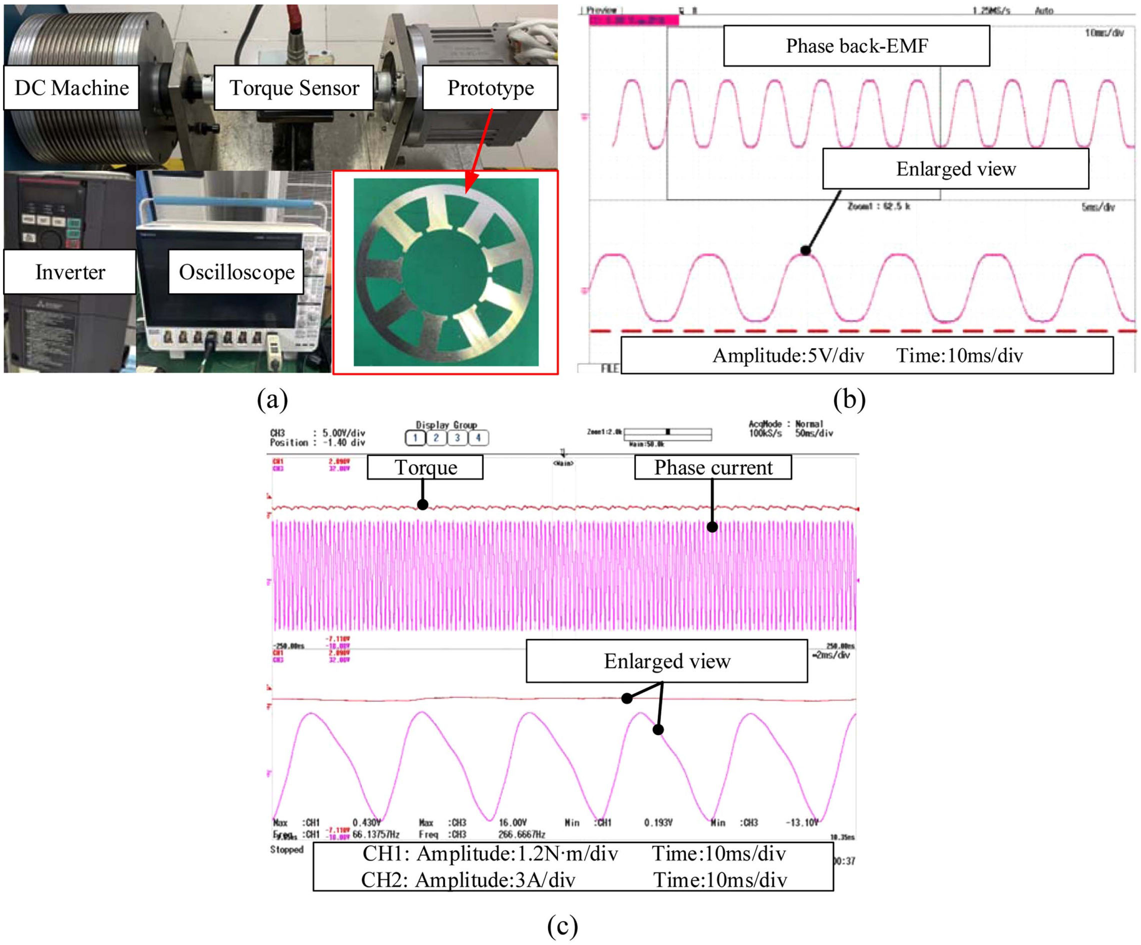

Fig. 11. (Color online) Experiment under the condition of 4000 rpm and 10A (a)Complete control system. (b) Measured back-EMF. (c) Measured current and torque.

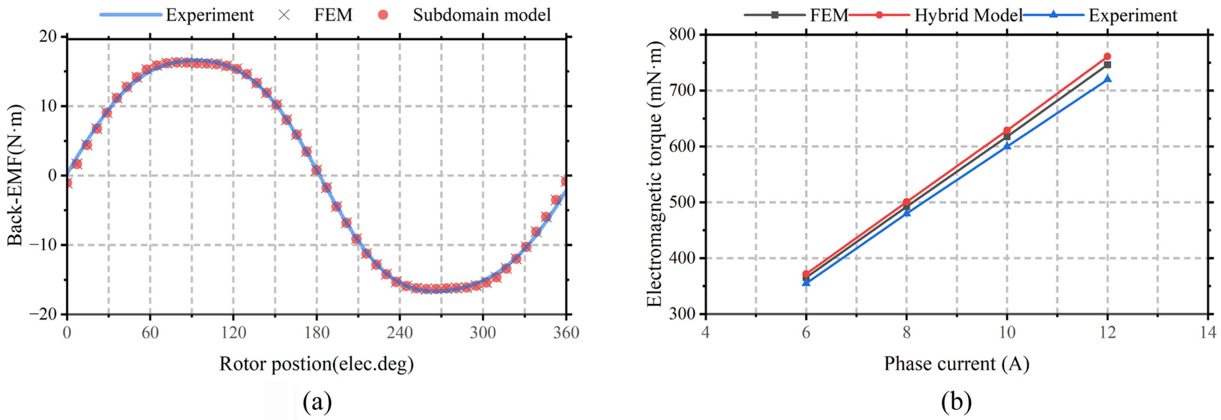

Fig. 12. (Color online) On-load comparison. (a) Back-EMF. (b) Electromagnetic torque versus phase current.

reaction and magnetic saturation is negligible. Therefore, the air-gap field can be calculated using the linear subdomain model without coupling with the magnetic network. Fig. 13 illustrates a comparison between the subdomain and FEM results for the no-load air-gap flux density and back-EMF. The consistency of each curve confirms that this simplification provides accurate and reliable predictions.

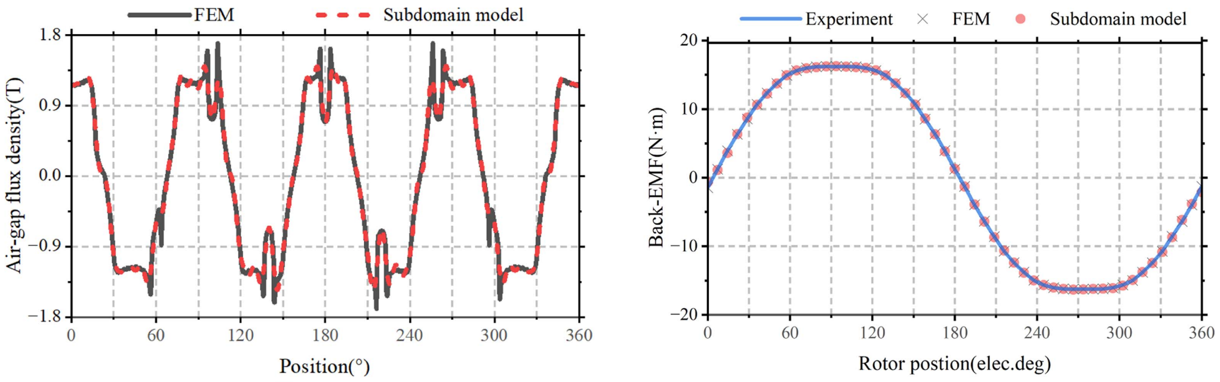

(a) (b)

Fig. 13. (Color online) No-load comparison. (a) Air-gap flux density. (b) Back-EMF.

Table 4. Required model updates under different design variations.

Design variation	Impact on analytical formulation	Required model update
Geometric parameter	No structural change	Update geometric parameters
Slot/Pole number	Minor subdomain and EMN adjustment	Update the geometric parameter and EMN nodes
Magnet topology	Subdomain redefinition	Redefine subdomains and boundaries
Material property	No structural change	Update EMN parameters
Machine type	Full reformulation	Rebuild analytical model
Irregular geometry	Not analytically describable	FEM required

5. Discussion

The developed hybrid analytical model can be classified as an analytical-numerical coupling approach. It combines the subdomain analytical formulation with a non-linear EMN. The subdomain model provides an analytical description of the air-gap field, while the EMN introduces the non-linear magnetic behavior of the iron core through iterative flux-MMF coupling. Compared with purely analytical models, the proposed approach takes magnetic saturation into account. Compared with numerical methods such as FEM, it achieves comparable accuracy under non-linear conditions with a much faster calculating. In essence, the hybrid model bridges the gap between analytical and numerical analysis. It maintains the physical transparency of analytical modeling while integrating non-linear magnetic effects through the EMN. This balance of accuracy, efficiency and physical interpretability highlights the superiority of the proposed model.

The quantitative results help clarify the scope and limitations of the proposed approach. As shown in Table 2, the deviation between the hybrid model and FEM remains very small for the dominant low-order harmonic, while larger discrepancies appear for higher-order harmonics. This indicates that the global magnetic field and its main components are well captured, whereas higher spatial harmonics are more sensitive to local effects. These discrepancies mainly originate from localized saturation and flux crowding near tooth tips and slot openings. Such effects are difficult to represent using lumped permeance elements and equivalent surface currents. From a practical perspective, the proposed model is well suited for rapid performance evaluation and parametric studies, where repeated simulations are required. It provides a favorable balance between computational efficiency and predictive accuracy. The model is limited to geometries that can be described by analytical boundaries, and it does not resolve highly localized saturation patterns. For cases involving strong local saturation, complex geometries, or detailed loss and thermal analysis, full finite-element simulations remain more appropriate. To clarify the applicability of the proposed approach under different design variations, Table 4 summarizes the required level of model update for typical changes encountered in electrical machine design.

Future work will focus on extending the formulation to handle more complex geometries through piecewise boundary descriptions and on improving the EMN by introducing locally adaptive permeance representations.

These developments are expected to enhance the ability of the model to capture localized saturation effects while preserving its computational efficiency.

6. Conclusion

This paper has proposed a hybrid analytical model for a SPM machine with Halbach magnet arrays by combining the subdomain model with the EMN model. The subdomain model is formulated by incorporating equivalent surface currents into the boundary conditions. The equivalent surface currents are further determined using the EMN model, which accounts for the B-H characteristics of the iron core. This hybrid approach allows the model to accurately capture the nonlinear saturation behavior of the iron core while maintaining high computational efficiency. Extensive validations have been conducted through both FEM and experimental measurements. The results confirm that the model can accurately predict critical electromagnetic performance indices, including air-gap flux density, torque characteristics, etc. In addition, the model demonstrates strong potential for design optimization and parameter sensitivity analysis due to its fast computation capability. Although a specific machine configuration is considered in this paper, the proposed hybrid analytical framework is parameter driven and can be readily extended to other pole–slot combinations and Halbach segmentation schemes through straightforward parameter updating, without modifying the model structure. Future work will focus on further extending the model to incorporate end-effect considerations, loss modeling, and temperature-dependent material properties, thereby enhancing its applicability to a wider range of high-performance PM machine designs with complex magnetization patterns.

Acknowledgments

This work was supported by the Research Program of Department of Education of Zhejiang Province (Y202559183).

References

[1] D. Egorov, I. Petrov, J. J. Pyrhönen, J. Link, R. Stern, P. Sergeant, and B. Sarlioglu, IEEE Trans. Ind. Electron. **69**, 121 (2022).

[2] J. Mao, X. Xu, Y. Tang, Y. Ren, J. Feng, and J. Zheng, J. Magn. **30**, 266 (2025).

[3] J. Chen, K. Liu, S. Zhou, H. Cai, Y. Chen, C. Huang, and D. Zhang, IEEE Trans. Ind. Appl. **60**, 5953 (2024).

[4] Z. Zhang, C. Wang, and W. Geng, IEEE Trans. Ind. Electron. **67**, 7269 (2020).

[5] Y. Du, J. Zhao, F. Xiao, X. Zhu, L. Quan, and F. Li, IEEE Trans. Veh. Technol. **70**, 3187 (2021).

[6] M. Shang, J. Liu, X. Chai, and M. Li, Proc. ICEMS **2024**, 3427 (2024).

[7] Y. Li, Z. Q. Zhu, S. Brockway, M. Manss, J. Lea, and Y. Ren, IEEE Trans. Ind. Appl. **61**, 7105 (2025).

[8] B. Tong, K. Wenguang, L. Chen, L. Jing, and X. Qi, J. Magn. **30**, 282 (2025).

[9] A. Mohammadi Ajamloo, A. Ghaheri, M. N. Ibrahim, and P. Sergeant, IEEE Trans. Transp. Electrific. **11**, 6392 (2025).

[10] M. Al-ani, A. Walker, G. Vakil, D. Gerada, C. Gerada, and K. Paciura, IEEE J. Emerg. Sel. Top. Power Electron. **11**, 2029 (2023).

[11] L. Jia, M. Lin, A. Yang, Y. Tu, and K. Lin, IEEE Trans. Appl. Supercond. **34**, 1 (2024).

[12] C. Chen, X. Wu, X. Yuan, and X. Zheng, IEEE Trans. Ind. Electron. **72**, 1325 (2025).

[13] Y. Fang, J. Ji, and W. Zhao, CES Trans. Electr. Mach. Syst. **6**, 413 (2022).

[14] Y. Ni, B. Cao, Q. Chen, Y. Huang, and Q. Wang, IEEE Trans. Transport. Electrific. **10**, 2936 (2024).

[15] Z. Song, C. Liu, K. Feng, H. Zhao, and J. Yu, IEEE Trans. Transp. Electrific. **6**, 1577 (2020).

[16] Y. Du, Y. Huang, B. Guo, F. Peng, and J. Dong, IEEE Trans. Transp. Electrific. **9**, 2891 (2023).

[17] B. Guo, Y. Wu, and F. Peng, IEEE Trans. Ind. Electron. **72**, 10487 (2025).

[18] M. Ghods, J. Faiz, M. A. Bazrafshan, H. Gorginpour, and M. S. Toulabi, IEEE Trans. Ind. Electron. **71**, 237 (2024).

[19] X. Zhu, G. Qi, M. Cheng, W. Qin, Y. Liu, and J. Huang, IEEE Trans. Transport. Electrific. **11**, 3538 (2025).

[20] W. Liu, H. Yang, H. Lin, and L. Qin, IEEE Trans. Ind. Electron. **69**, 1739 (2022).

[21] M. Shen, P.-D. Pfister, C. Tang, and Y. Fang, IEEE Trans. Magn. **57**, 1 (2021).

[22] L. J. Wu, Z. Q. Zhu, D. Staton, M. Popescu, and D. Hawkins, IEEE Trans. Magn. **47**, 1693 (2011).

[23] D. Cao, W. Zhao, J. Ji, L. Ding, and J. Zheng, IEEE Trans. Energy Convers. **34**, 1950 (2019).